

See discussions, stats, and author profiles for this publication at: <https://www.researchgate.net/publication/384423076>

Investigation of Zr doping and Electrochemical study on $\text{Li}_{1+x}\text{Ta}_{1-x}\text{Zr}_x\text{SiO}_5$ ($x = 0 - 0.3$) Solid Electrolyte for Lithium-Ion Battery

Article in Journal of Electrochemical Science and Technology · September 2024

DOI: 10.33961/jecst.2024.00773

CITATIONS

0

READS

68

6 authors, including:



Ramkumar Balasubramaniam

University of Ulsan

12 PUBLICATIONS 153 CITATIONS

SEE PROFILE



Anjali Anilkumar

Chonnam National University

1 PUBLICATION 0 CITATIONS

SEE PROFILE



Vanchiappan Aravindan

Indian Institute of Science Education and Research, Tirupati

301 PUBLICATIONS 17,096 CITATIONS

SEE PROFILE

Investigation of Zr doping and Electrochemical study on $\text{Li}_{1+x}\text{Ta}_{1-x}\text{Zr}_x\text{SiO}_5$ ($x = 0 - 0.3$) Solid Electrolyte for Lithium-Ion Battery

Yeong-A Kim^a, Ramkumar Balasubramaniam^a, Anjali Anilkumar^a, Vanchiappan Aravindan^b,
Sangho Park^c, Yun-Sung Lee^{a,*}

^a School of Chemical Engineering, Chonnam National University, Gwangju 61186,
Republic of Korea

^b Department of Chemistry, Indian Institute of Science Education and Research (IISER),
Tirupati - 517507, India

^c School of Chemical Engineering, Jeonbuk National University, Jeonju 54896, Republic of
Korea

Corresponding authors: E-mail: leeys@chonnam.ac.kr

Abstract

Materials with high lithium-ion conductivity are promising for use as electrolytes in solid-state batteries. However, several technical challenges, such as stability in air and optimal synthetic conditions, inhibit their extensive application. In this study, LiTaZrSiO_5 solid electrolytes (SEs) are prepared at different sintering temperatures (900–1100 °C) and characterized using X-ray diffraction, scanning electron microscopy, and electrochemical impedance spectrometry. Correlations among the sintering temperature, structural properties, and ionic conductivity of the LTZO SEs are examined systematically and discussed. According to the results, high ionic conductivity can be achieved by optimizing the sintering temperature of the SEs. The LTZO SE sintered at 1050 °C exhibited the highest ionic conductivity. To further improve ionic conductivity, the sintering time was optimized in the range of 6–24 h. The conductivity improved as the sintering time increased from 6 to 12 h, and the best conductivity was achieved at 12 h. For sintering durations longer than 12 h, the conductivity of the material decreased. Further, doping emerged as a prominent strategy for increasing the ionic conductivity of the SEs. The effects of different concentrations of Zr dopant on the physio-chemical (structural, morphological) and electrochemical properties of the $\text{Li}_{1+x}\text{Ta}_{1-x}\text{Zr}_x\text{SiO}_5$ ($x=0-3$) SEs were investigated. Compared to the results obtained for the other SEs, extraordinary results were obtained by doping the $\text{Li}_{1.1}\text{Ta}_{0.9}\text{Zr}_{0.1}\text{SiO}_5$ SE with zirconium, such as increased ionic conductivity, reduced charge transfer resistance, reduced crack formation, and increased SE particle size. In sum, the sintering temperature, sintering time, and dopant concentration in the synthesized $\text{Li}_{1+x}\text{Ta}_{1-x}\text{Zr}_x\text{SiO}_5$ ($x = 0-3$) precursors should be optimized to promote the development of LTZSO electrolytes suitable for use in future SSBs.

Keywords:

Solid electrolyte; Sintering temperature; Sintering time; Doping concentration; Lithium ionic conductivity

1. Introduction

Development of advanced sustainable lithium-ion batteries (LIBs) is necessary to mitigate the problems of environmental degradation and greenhouse effect, and reduce the consumption of natural energy resources. [1,2,3,4,5] In recent decades, LIBs have been extensively used in portable electronics, electric vehicles, electronic gadgets, and energy storage devices because of their high energy density, storage capacity, long lifespan, and light weight. [1,2,3,4,6,7,8,9,10,11,12] Nevertheless, typical LIBs continue to be affected by safety hazards, such as Li-dendrite formation, explosions resulting from the use of combustible organic solvents, electrolyte leakage, and undesirable side reactions. [8,9] Therefore, the use of solid electrolytes (SE) has been investigated to solve the safety issues caused by the leakage of flammable organic liquid electrolytes (LEs) in conventional LIBs. [1,7,9,13,14,15] Solid-state batteries (SSBs) have attracted considerable interest in recent years, especially for use in modern electric vehicles (EVs). Among the different materials used in such batteries components, the SE is the most reactive and complex material, and it considerably influences SSB failure. Therefore, the development of a highly conductive and stable SE is critical to the success of SSBs.

Many studies have focused on improving the structural stability and conductivity performance of SEs. Generally, garnet $\text{Li}_7\text{La}_3\text{Zr}_2\text{O}_{12}$, NASICON ($\text{Li}_{1+x}\text{Al}_x\text{Ti}_{2-x}(\text{PO}_4)_3$, LATP), perovskite-type ($\text{Li}_{3x}\text{La}_{0.67-x}\text{TiO}_3$, LLTO), $\text{Li}_{10}\text{GeP}_2\text{S}_{12}$ family, and argyrodite sulfide-based SEs are used in SSBs. [16,17,18,19,20,21,22,23] However, many of these SEs are unstable against air or Li metal. [1,7,13,24] Therefore, new Li-ionic conductors that offer both remarkable ionic conductivity and excellent stability need to be developed as SEs for SSBs. To achieve high ionic conductivity, from the crystal structure perspective, research is being conducted to achieve the lowest Li-ion migration barrier. [25,26,27] For example, materials with a body-centered cubic (BCC)-like anion framework structure exhibit high ionic conductivity owing to the low activation energy required for Li-ion movement. [25] However, despite considerable research, the only materials with a BCC-like anion framework structure are LGPS and $\text{Li}_7\text{P}_3\text{S}_{11}$, which are sulfide-based SEs. [25] Although, garnet- and NASICON-structure-based oxide SEs are grouped under non-BCC-like anion framework materials, they provide higher ionic conductivity. [25,26] This is because certain element doping compositions within the crystal can induce a disordered Li-ion sublattice that helps ions move quickly by using the repulsive forces between adjacent ions. [26,27] However, the characteristic of the crystal structure framework of SEs that causes this higher ionic conductivity remains controversial.

Recently, Mo et al. reported a computational model of fast ion diffusion in Li superionic conductors (LICs) to explain the concerted migration of multiple Li ions. [26] Theoretically, this model is based on the strategy of inserting Li-ions into high-energy sites to initiate concerted ion migration with a lower energy barrier. [26] Based on this knowledge, Chen et al. and Guo et al. prepared a new SE called LiTaSiO₅ (LTSO) by using quenching and the solid-state method. [24, 28] Chen et al. studied the structure and Li-ion diffusion mechanism of Li_{1+x}Ta_{1-x}Zr_xSiO₅ ($0.5 \geq x \geq 0$) by using the ab-initio molecular dynamic (AIMD) simulation method. [24] Guo et al. studied the crystal structure, electrical properties, and Li-ion migration pathways of LiTaSiO₅ and Li_{1.1}Ta_{0.9}Zr_{0.1}SiO₅ by performing AIMD stimulations. [28] They proposed a monoclinic structure with the space group P 21/c (No.14). [29] According to the literature, the LiTaSiO₅ crystal structure is composed of an the SiO₄ tetrahedron and a corner-sharing TaO₆ octahedron. The Li-ions occupying the 4e tetrahedral sites and the LiO₄ tetrahedrons share edges with adjacent SiO₄ and TaO₆ polyhedrons. [24, 26, 28, 29] This 3D framework with a suitable bottleneck size is suitable for Li-ion transfer from the perspective of accomplishing concerted Li-ions migration. Furthermore, these studies demonstrated that the high ionic conductivity of the material at room temperature is due to zirconium (Zr) doping. The Zr⁴⁺ (0.72 Å) ionic radius is higher than Ta⁵⁺ (0.64 Å) and it assists to increase the lattice parameters of the SEs. [24, 30] Additionally, the excess lithium is added to composition to compensate the doping of Zr⁴⁺ instead of Ta⁵⁺. The excess lithium is beneficial for the ionic conductivity of the electrolyte.

The preparation methods used in these works were almost similar to the solid-state reaction described in a previous report. [28] Nonetheless, comprehensive and extensive focus on the preparation of LTSO SE is highly desirable for comprehending the effect on the phase formation and ionic conductivity of LTSO. In the present work, we report the preparation of Li_{1+x}Ta_{1-x}Zr_xSi_xO₅ ($x = 0-3$) by using the conventional solid-state method. The prepared LTSO SE is sintered at different temperatures and for different durations to evaluate the effects of these variables on its structure, morphology, and ionic conductivity. We systematically investigate the effect of sintering temperature, time, and doping concentration on the structural formation, surface morphology and conductivity performance of the prepared LTSO SEs.

2. Experimental section

2.1 Preparation of $\text{Li}_{1+x}\text{Ta}_{1-x}\text{Zr}_x\text{Si}_x\text{O}_5$ ($x = 0-3$) SEs

$\text{Li}_{1+x}\text{Ta}_{1-x}\text{Zr}_x\text{Si}_x\text{O}_5$ ($x = 0-3$) compounds were prepared using a ball-milling method (PULVERISETTE 6 Planetary Mono Mill). In this process, lithium carbonate (Li_2CO_3 , Sigma Aldrich, USA), tantalum pentoxide (Ta_2O_5 , DAEJUNG, Korea), zirconium oxide (ZrO_2 , Sigma Aldrich, USA), and silicon oxide (SiO_2 , Sigma Aldrich, USA) were used as the starting materials. To compensate for lithium loss at high temperatures during synthesis, the compounds were prepared with 5 wt.% excess Li_2CO_3 . The precursors were mixed in stoichiometric amounts with ethanol in a ball milling jar and wet mixed at 200 rpm for 6 h until a fine homogeneous mixture was obtained. Thereafter, the solvent was evaporated, and the mixture was dried in an oven at 50 °C for 12 h. The powders obtained after drying were calcined at 650 °C for 12 h in air atmosphere. The calcined powders were cold pressed under a pressure of 100 MPa to obtain pellets with a thickness of approximately 1 mm and diameter of 10 mm. Lastly, the final product $\text{Li}_{1+x}\text{Ta}_{1-x}\text{Zr}_x\text{Si}_x\text{O}_5$ ($x=0-3$) was synthesized by sintering the pellets at 900 °C for 6–24 h in air atmosphere.

2.2 Material and electrochemical characterizations of $\text{Li}_{1+x}\text{Ta}_{1-x}\text{Zr}_x\text{Si}_x\text{O}_5$ ($x = 0-3$) SEs

A high-resolution X-ray diffraction (HR-XRD) analyzer was used to determine the crystal structure of the sintered sample. The Bragg's equation can be used to calculate the lattice spacing (d) of the electrolyte. [31]

$$n \lambda = 2 d \sin \theta$$

Where the λ is the X-ray wavelength (0.15418 nm) and θ is the Bragg's diffraction angle. The average grain size of the electrolyte is calculated using the Debye-Scherrer equation. [4,31]

$$D = \frac{K \cdot \lambda}{FWHM (2\theta) \cdot \cos(\theta)}$$

K is the Scherrer constant (0.9) and β is the full-width at half maximum (FWHM).

The surface morphology and particle size of the synthesized $\text{Li}_{1+x}\text{Ta}_{1-x}\text{Zr}_x\text{Si}_x\text{O}_5$ ($x=0-3$) SE were confirmed using field emission scanning electron microscopy (FE-SEM). Inductively coupled plasma luminescence analysis (ICP-OES, Inductively Coupled Plasma Optical Emission Spectroscopy) was performed to study the stoichiometry of the sample. Its ionic

conductivity was measured using an electrochemical impedance spectrometry analyzer (EIS, LCR meter 4284A, HP Co., USA) in the frequency range of 1 MHz–25 HZ. A thin layer of Pt was sputtered on each surface of the sintered pellets as an electrolyte. Ion conductivity was calculated using the equation $\sigma = d / (A \times R)$, where d is the pellet thickness (0.1 cm), A is the contact area of the pellet, and R is the total resistance value measured using EIS.

3. Results and discussion

3.1. Optimization of sintering temperature of LiTaSiO₅ (LTSO) SE

3.1.1. Analysis of Structural Characteristics of LiTaSiO₅ (LTSO) SE by Optimizing the Sintering Temperature

Sintering conditions such as temperature, time, and atmosphere of the sintering process are important factors affecting the structural and electrochemical characteristics of SEs. [32] Therefore, it is important to optimize the sintering conditions for synthesizing the SE. In addition, such optimization is necessary to prevent unwanted side effects, such as Li-loss during the sintering process and optimization of sample composition. As the primary heat treatment, LiTaSiO₅ SE pellets were sintered in a box furnace in air atmosphere for 6 h at temperatures of 900 °C to 1100°C, where the temperature was increased in steps of 50 °C, to check the optimum synthesis conditions.

X-ray diffraction analysis was performed to determine the structural characteristics of the samples sintered under various sintering temperature conditions. **Figure 1a** depicts the XRD patterns of the LTSO SEs sintered at different temperatures ranging from 900°C to 1100°C. The XRD patterns of the sample sintered at 900°C and 950°C did not match the reference pattern (ICSD#39648). [27] This result was attributed to the failure to bind the oxygen atoms and silicon atoms during synthesis of the LiTaSiO₅ SE under low-temperature conditions. As depicted in Figure 1a, the diffraction peaks of the pristine LTSO powder at 1000°C or higher belong to a monoclinic phase, confirming that the LTSO structure clearly changes from the trigonal phase (space group: P 1, LiTaO₃) to the monoclinic phase with increasing sintering temperature. This result indicated that the sintering temperature had a significant effect on the crystal structure and phase formation of the LTSO SE. Additionally, a minor impurity phase (LiTaO₃) was detected in all LTSO powders sintered at high temperatures.

Figure 1b depicts the XRD pattern of the (110) plane of the LTSO SE obtained by

sintering at 1000–1100°C. For the pellets sintered at 1000–1050°C, the (110) peak intensities increased. However, for the pellets sintered at 1100°C, the peak intensities and d-spacing values decreased (**Figure 1c**). This indicated that LTSO might have undergone lithium evaporation at around 1100°C. For clarity, the lattice parameters of the samples sintered at different temperatures are summarized in **Table 1**. The lattice parameters and volume of the LTSO SE were higher only at the sintering temperature of 1050°C. Seemingly, the lattice parameters of the sample sintered at 1100°C were marginally lower, possibly because of lithium loss.

3.1.2. Morphological and Electrochemical Characteristics of LiTaSiO₅ (LTSO) SE by Optimizing the Sintering Temperature

Electrochemical impedance spectroscopy (EIS) was performed to study the ionic conductivity of the LiTaSiO₅ SE as a function of the sintering temperature in the range of 900°C–1100°C. The Cole-Cole plots of all the sintered samples exhibit only one semicircle in the high-to-low-frequency region (**Figure 1d**). The semicircle in the graph is related to the total impedance of grains and grain boundaries. Compared to the resistance of the low-temperature sample, the resistance of the high-temperature samples was lower, and it decreased and then increased as the sintering temperature increased. Li evaporation during long-term sintering may have led to an increase in charge transfer resistance. [4,33] The ionic conductivity of the SE samples at RT increased as the sintering temperature increased, and it reached approximately $7.76 \times 10^{-8} \text{ S cm}^{-1}$ for the LTSO SE sintered at 1050 °C. However, the ionic conductivity of the sample sintered at 1100 °C was lower. The sample sintered at 1050 °C exhibited the smallest grain boundary resistance value (2,090,000 Ω) in the EIS curve, and this result was attributed to its higher d-spacing value and lattice parameter, as confirmed by XRD analysis (**Figures 1 a–c**). Hence, the sintering temperature of 1050 °C was selected as a suitable condition for further synthesis of LTSO SEs.

FE-SEM was used to examine the surface morphology of the LTSO SEs pellets. **Figures 2a–d** present morphological images of the LTSO pellets prepared by sintering at 900–1100°C. The images in Figures 2 a, b confirm that sintering at 900–950°C was inadequate for particle binding. According to **Figure 2c**, at the sintering temperature of 1000°C, the interparticle contact area increased due to neck growth, and a continuous pore channel was developed in the pellets. [34,35,36,37] At the sintering temperatures of 1050–1100°C, this continuous pore channel vanished owing to particle fusion, and large pores in the pellets were eliminated because the particle size increased (**Figure 2d**). [34,35,36,37] Additionally, cracks were

observed in all the pellets sintered at high temperatures. Hence, sintering at temperatures exceeding 1000°C was confirmed to have increased the pellet's compaction strength and integrity.

3.2. Optimization of sintering time of LiTaSiO₅ (LTSO) SE

3.2.1. Analysis of Structural Characteristics of LiTaSiO₅ (LTSO) SE by Optimizing the Sintering Time

The XRD patterns of the LTSO SEs sintered at 1050 °C for durations of 6 h to 24 h are presented in **Figure 3**. These XRD results exhibit characteristic peaks, and there are no significant differences in the crystallinity of the samples prepared by sintering for 6 h to 18 h (**Figure 3a**). **Table 2** summarizes the lattice parameters of the samples prepared by sintering for different durations. As the sintering time increased from 6 h to 12 h, the average grain size of the samples increased owing to grain boundary migration. [32,38] In samples sintered for more than 12 h, the average grain size decreased owing to enhanced grain boundary generation. [39] **Table 3** summarizes the average grain sizes of the samples sintered for different durations. The peak intensity of the sample sintered for 24 h decreased owing to Li evaporation (**Figure 3b**). In addition, LiTaO₃ impurity peaks were identified in the spectra of all the prepared samples owing to inadequate bonding between oxygen and silicon atoms.

3.2.2. Morphological and Electrochemical Characteristics of LiTaSiO₅ (LTSO) SE by Optimizing the Sintering Temperature

Figure 3d shows the Cole-Cole plot of the LTSO SEs sintered for different durations (6–24 h). In **Figure 3d**, a correlation is established between the sintering time and resistance properties of the LTSO SEs. As the temperatures increased, the diameter of the semicircle decreased steadily, and simultaneously, ionic conductivities of the LTSO SEs increased. The total resistance (R_{total}) of the LTSO SEs decreased as the sintering time increased from 6 to 12 h. The total resistance of the LTSO SEs first decreased from 6 h to 12 h then increased as the holding time reached 18 h, as can be inferred from their microstructural properties and grain size data (Table 3). The samples sintered at 1050 °C for 12 h exhibited the highest ionic conductivity ($1.78 \times 10^{-7} \text{ S cm}^{-1}$), which was attributed to its lowest total resistance (1,350,000 Ω), highest d-spacing (110 plane) value, and improved crystallinity (**Figure 3b-c**). Apart from sintering temperature, sintering time, too, significantly influenced Li⁺ volatilization. As the sintering time increased (> 18h), the volatilization of Li⁺ in the LTSO SEs was unavoidable,

which could have led to a decrease in peak (110) intensity (**Figure 3b**). When the holding time was short (12 h), the conductivity of the LTSO SEs increased owing to the large average grain size and low intensity of the LiTaO_3 phase. However, the conductivity of the LTSO SEs decreased as the holding time increased beyond a certain threshold (>12 h), probably because of Li^+ volatilization and an increase in LiTaO_3 phase intensity (**Figure 3a**). Accordingly, prolonged sintering times adversely affected the ionic conductivity of the SEs. Therefore, the sintering time of 12 h was selected as the optimal condition for further processing.

The morphological images presented in **Figure 4** systematically reveal the effect of sintering time on the sintered LTSO SE pellets. Additionally, the porosity of the LTSO pellets decreased significantly as the sintering holding time increased. No major transformation in particle shape occurred with increasing sintering time. Moreover, all the samples exhibited crack formation owing to thermal expansion of particles.

3.3. Optimization of doping concentration of $\text{Li}_{1+x}\text{Ta}_{1-x}\text{Zr}_x\text{SiO}_5$ ($x = 0 - 0.3$) SE

3.3.1. Analysis of Structural and Morphological Characteristics of $\text{Li}_{1+x}\text{Ta}_{1-x}\text{Zr}_x\text{SiO}_5$ ($x = 0 - 0.3$) SE by Optimizing the doping concentration

An ICP-OES analysis was performed to check the actual stoichiometry of the $\text{Li}_{1+x}\text{Ta}_{1-x}\text{Zr}_x\text{SiO}_5$ ($x = 0 - 0.3$) SEs, and the results are summarized in **Table 5**. The ICP-OES analysis was carried out after pre-treating the SE samples with aqua regia. For five SE compositions, most of the target values of the synthesis materials and the values obtained through analysis were consistent.

The XRD patterns of the Zr-doped $\text{Li}_{1+x}\text{Ta}_{1-x}\text{Zr}_x\text{SiO}_5$ ($x = 0 - 0.3$) powders are presented in **Figure 5a**. In the composition range of $x = 0-0.2$, the diffraction patterns were indexed based on the reference pattern (ICSD#39648) with a small amount of LiTaO_3 impurity phase. For $x = 0.1$ or higher, the major (110) diffraction plane shifted to a lower degree, meaning that Zr^{4+} was successfully incorporated into the crystal structure, and the d-spacing and lattice parameter values increased, which favored fast Li-ion transfer (**Figure 5b-c**). **Table 4** summarizes the lattice parameters of the prepared $\text{Li}_{1+x}\text{Ta}_{1-x}\text{Zr}_x\text{SiO}_5$ ($x = 0-0.3$) electrolyte. The diffraction peaks shifted to lower angles owing to the larger ionic radius of Zr^{4+} (0.72 Å) than that of Ta^{5+} (0.64 Å) [24, 30]. However, as the zirconium substitution composition value x increased, the LiTaO_3 peak intensified, which was attributed to destabilization of the binding of oxygen and silicon due to zirconium substitution. Additionally, for $x = 0.3$, a new ZrSiO_4

peak evolved in the sample. [40, 41] Therefore, the zirconium substitution composition range for maintaining the LiTaSiO₅ crystal phase was set to $x = 0-0.2$. The morphology of the as-synthesized Zr-doped Li_{1+x}Ta_{1-x}Zr_xSiO₅ ($x = 0 - 0.3$) SE powders sintered at 1050 °C for 12 h in the air is depicted in Figure 6. zirconium content played a critical role in decreasing cracking and porosity of the pellets. Furthermore, zirconium doping improved contact between the SE particles. This reduced cracking and increased the relative density of the pellets. This phenomenon can be viewed from various perspectives. Solid-state diffusion plays a significant role in particle formation and interparticle bonding, and therefore, diffusion-based bonding has a vital effect on the mechanical and microstructural properties of materials. [42, 43, 44] Furthermore, diffusion itself is governed by sintering temperature and time. [42, 43, 44] Consequently, the relative density of the Li_{1+x}Ta_{1-x}Zr_xSiO₅ ($x = 0 - 0.3$) SEs decreased when the zirconium content was higher than $x = 0.1$. The large particle size of the SEs was attributed to the migration of boundaries. [32] Furthermore, the large particle size reduced the contact area between the SE particles, leading to lower density. [32, 42] High zirconium doping concentrations induced discontinuous grain growth. According to these results, particle size growth was directly proportional to doping concentration. In addition, the ionic conductivities of the Li_{1+x}Ta_{1-x}Zr_xSiO₅ ($x = 0 - 0.3$) pellets prepared with different zirconium doping concentrations were determined by performing an EIS analysis.

3.3.2. Electrochemical Characteristics of Li_{1+x}Ta_{1-x}Zr_xSiO₅ ($x = 0 - 0.3$) SE by Optimizing the doping concentration

A Cole-Cole plot of the Li_{1+x}Ta_{1-x}Zr_xSiO₅ ($x = 0-0.3$) SEs sintered at 1050 °C for 12 h is presented in **Figure 5d**. As depicted in this figure, a semicircle similar to that mentioned in the preceding sections was observed. For $x = 0$ and 0.05, the SEs exhibited low Li-ionic conductivities of 1.78×10^{-7} and 2.97×10^{-7} S cm⁻¹, respectively, owing to the lower density, d-spacing (110 plane) value, and lattice parameters (**Table 4**). As the Zr concentration increased, the total resistance value decreased at first and then increased, reaching a minimum at $x = 0.10$ ($R_{\text{tot}} = 11,500 \Omega$). The total ionic conductivity of Li_{1+x}Ta_{1-x}Zr_xSiO₅ was 2.01×10^{-5} S cm⁻¹. For comparison, the ionic conductivity properties of the LTSO SEs are summarized in **Table 6**. The heterovalent substitution of Zr⁴⁺ for Ta⁵⁺ could increase the lithium-ion concentration to accommodate charge compensation. In a similar manner, it may reduce the activation energy and, additionally, induce concerted diffusion to improve Li⁺ ionic conductivity. [24, 27, 28] Zr

doping in the LTZO SEs enhanced their ionic conductivities to up to 10^{-5} S cm⁻¹, which is two times higher than those of the pristine LTZO SEs (1.78×10^{-7} S cm⁻¹). This improvement was ascribed to the reduction of pores and cracks, as well as to the denser structure of the Li_{1.1}Ta_{0.9}Zr_{0.1}SiO₅ SE. Nevertheless, the conductivity of the Li_{1+x}Ta_{1-x}Zr_xSiO₅ ($x = 0-0.3$) SEs decreased as the doping concentration exceeded a certain value ($x > 0.1$), which was undoubtedly attributed to an increase in the LiTaO₃ peak intensity, decreasing density, and abnormal particle size growth (**Figure 6**) triggered by the generation of a new ZrSiO₄ phase (**Figure 5a**).

The ionic conductivities and relative densities of the Li_{1+x}Ta_{1-x}Zr_xSiO₅ ($x = 0-0.3$) SEs are summarized in **Table 6**. Compared to the pristine LTZO SEs (relative density of 79.5%), the relative densities of the Zr-doped LTZO SEs were higher (in excess of 90%), which first increased and then decreased with increasing doping concentration. It is well established that zirconium doping of LTZO SEs improves their conductivity and mechanical strength, in addition to reducing their resistance. In addition, it was concluded that sintering temperature (1050 °C), time (12 h), and zirconium substitution ($x = 0.1$) conditions increased the relative density and reduced cracking, which helped improve the ionic conductivities of the doped LTZO SEs by 250 times compared to those of the pristine LTZO SEs. Nevertheless, the ionic conductivities of the doped LTZO SEs were lower than the theoretical value of 6.4×10^{-3} S cm⁻¹ calculated through simulation. This was attributed to surface cracks, crystalline collapse, presence of LiTaO₃, and changes in particle size during the sintering process. Therefore, the optimization of process variables such as sintering temperature and time, substitution composition, substitution element changes, pressure required for pellet production, particle size, and density should be explored in future studies.

Figure 7 shows the Galvanostatic charge-discharge, Cyclic voltammetry, and Charge-discharge performance of the LTZSO SE cells. The working current density of the cell was 0.1 mA/cm² for the corresponding plating and stripping process and the duration time was 30 min. **Figure 7a** confirms there was no fluctuations during the cell performance and the electrolyte is stable up to 100 cycles. We added liquid electrolyte at the interface to improve the contact between electrolyte the Li metal electrode. The CV diagram (**Figure 7b**) shows clear oxidation and reduction peaks corresponding to lithium intercalation and de-intercalation in the NCM811 cathode. After the first cycle, the oxidation and reduction potential of the cell was shifted to lower potential due to the activation process. From **Figure 7c and 7d**, the initial

charge and discharge capacity of the cell were 123 and 99 mAh g⁻¹, respectively. Subsequently after the first cycle, the discharge capacity of the cell was increased due to the activation effect in the electrode/electrolyte interface. Afterwards 15 cycles, the cell provided a discharge capacity of 150 mAh g⁻¹. Moreover, we are working to improve the ionic conductivity, capacity and cell performance.

4. Conclusion

We successfully synthesized Li_{1+x}Ta_{1-x}Zr_xSiO₅ SE by using ball milling and optimized the synthesis by adjusting the sintering temperatures, sintering time, and doping composition. In XRD results of the prepared electrolytes, a few LiTaO₃ impurity peaks were observed at all sintering temperatures. In terms of total Li-ion conductivity, the highest value of 7.76×10^{-8} S cm⁻¹ was achieved by the sample sintered at 1050 °C for 6 h. The grain boundary resistance of the SEs decreased at first and then increased as the sintering time exceeded 12 h. Excessive sintering time led to structural instability owing to particle expansion and crystalline collapse, and the optimal sintering time of the LTZO SEs was 12 h. Zr doping played a crucial role during sintering of the packed calcined powders and in stabilizing the SE structure. After sintering, Zr⁴⁺ was successfully incorporated into the Li_{1+x}Ta_{1-x}Zr_xSiO₅ phase. In terms of optimization of the substitution composition, for $x = 0.3$, the crystalline phase collapsed, and the proportion of LiTaO₃ impurities increased; additionally, a ZrSiO₄ peak was generated. After Zr incorporation, the resistance value of the Li_{1.1}Ta_{0.9}Zr_{0.1}SiO₅ SE decreased, and it exhibited a high Li-ion conductivity of 2.01×10^{-5} S cm⁻¹ with a relative density of 90.7%. To further improve the ionic conductivity of the SE, process variables such as sintering conditions, dopant composition, pellet production pressure, particle size, and density should be optimized.

Acknowledgments

This work was supported by the National Research Foundation of Korea (NRF) grant funded by the Korean government (Ministry of Science, ICT & Future Planning) (No. RS-2023-00208361).

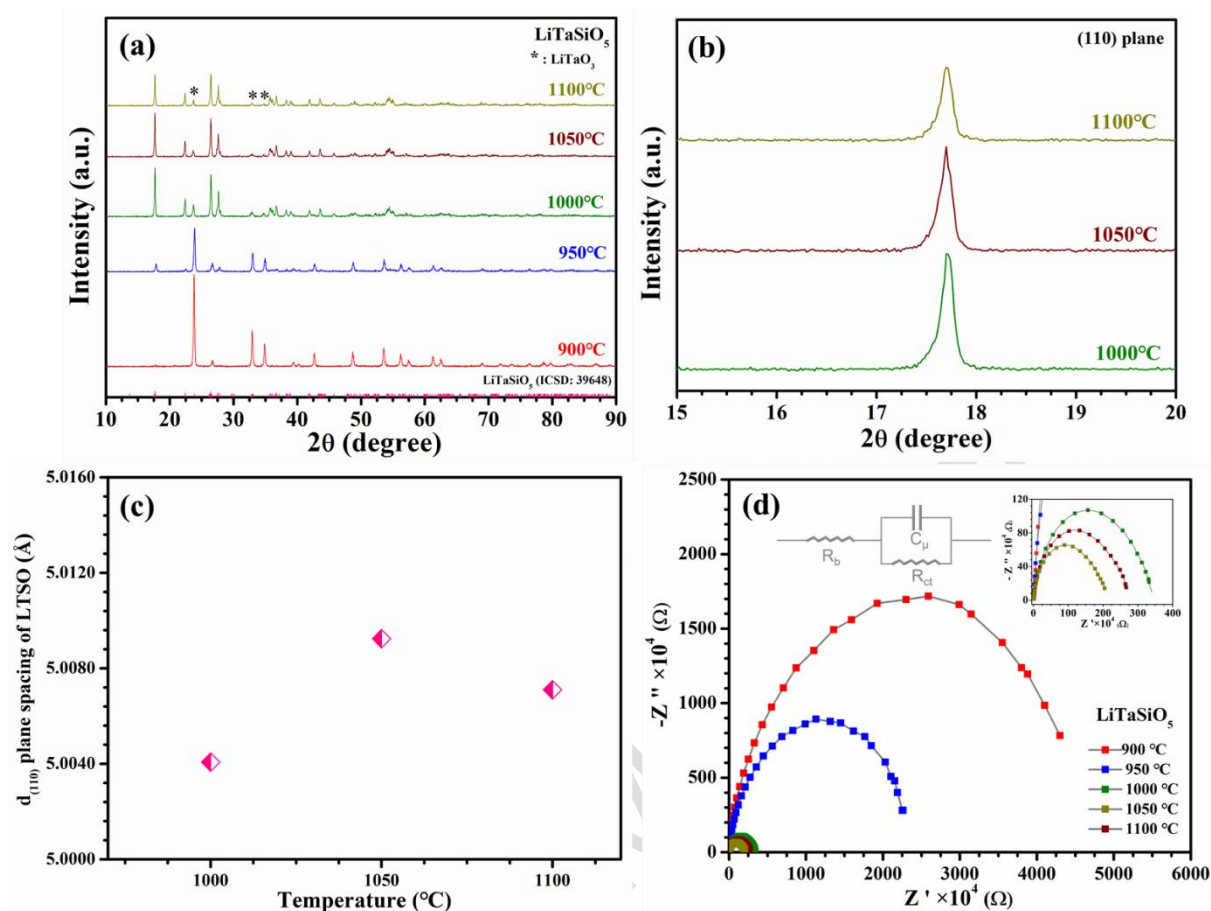


Figure. 1. (a) XRD patterns of LiTaSiO₅ SEs at different synthetic temperatures, (b) graph of the (110) plane intensity, (c) $d_{(110)}$ plane spacing of LiTaSiO₅ SEs at different temperatures, and (d) EIS curves of LiTaSiO₅ SEs prepared/sintered at different temperatures.

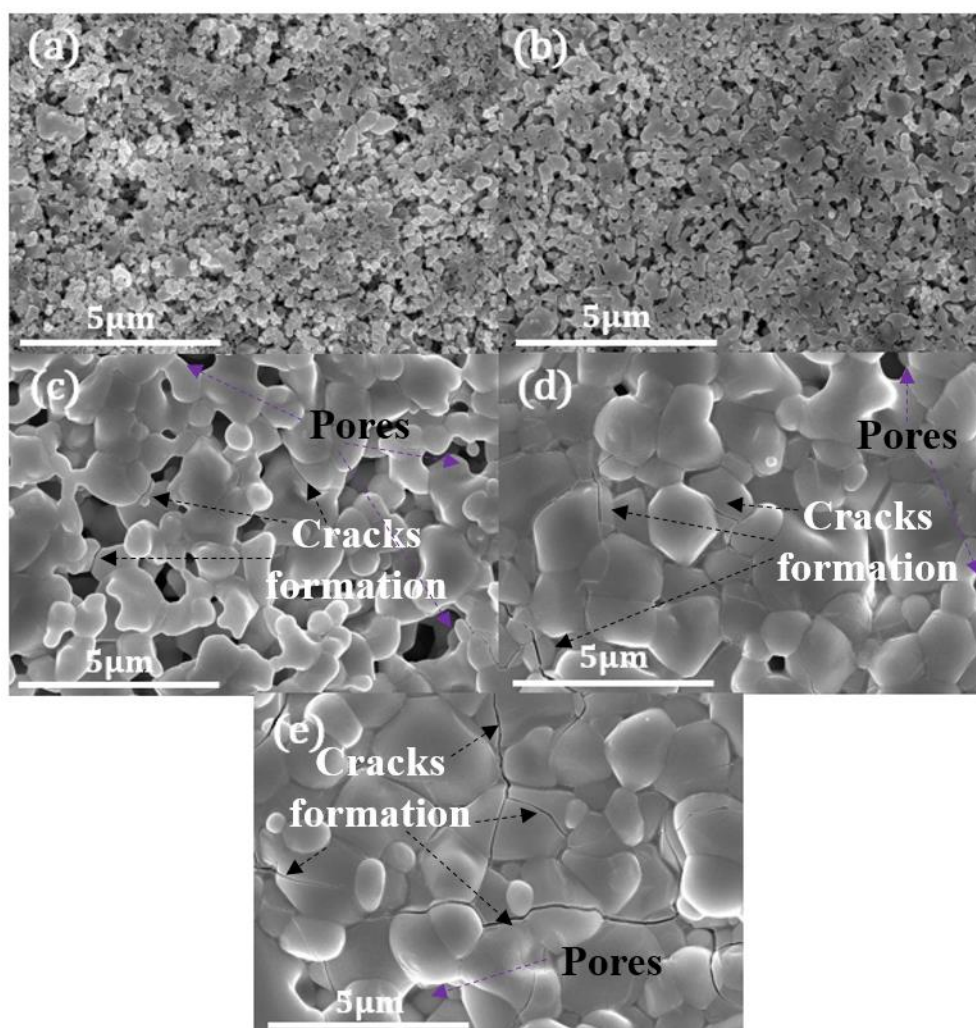


Figure. 2. FE-SEM images of LiTaSiO₅ SEs prepared by sintering at (a) 900 °C, (b) 950 °C, (c) 1000 °C, (d) 1050 °C, and (e) 1100 °C.

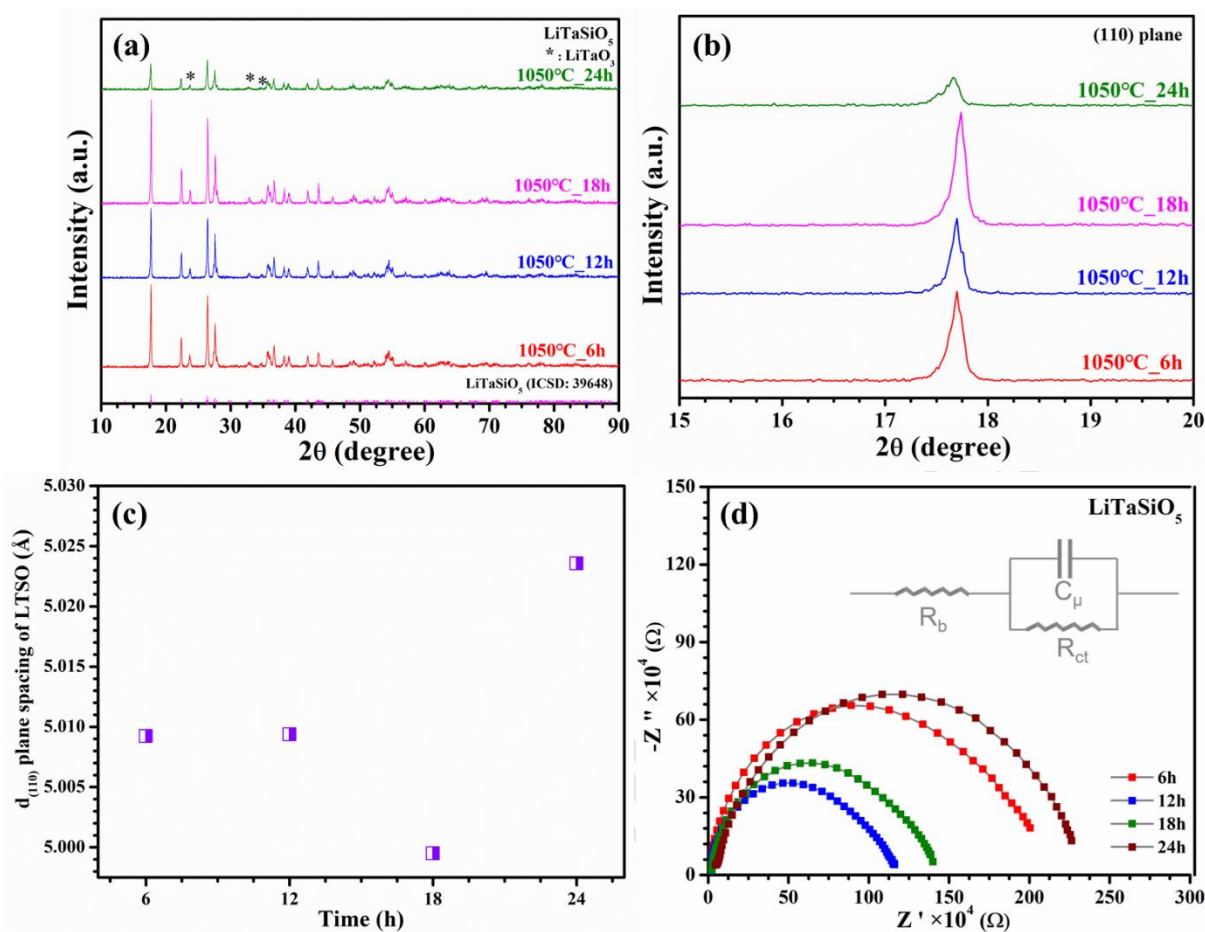


Figure. 3. (a) XRD patterns of LiTaSiO₅ SEs sintered for different durations, (b) graph of (110) plane, (c) d₍₁₁₀₎ plane spacing of LiTaSiO₅ SEs sintered for different durations, and (d) EIS curves of LiTaSiO₅ SEs sintered for different durations.

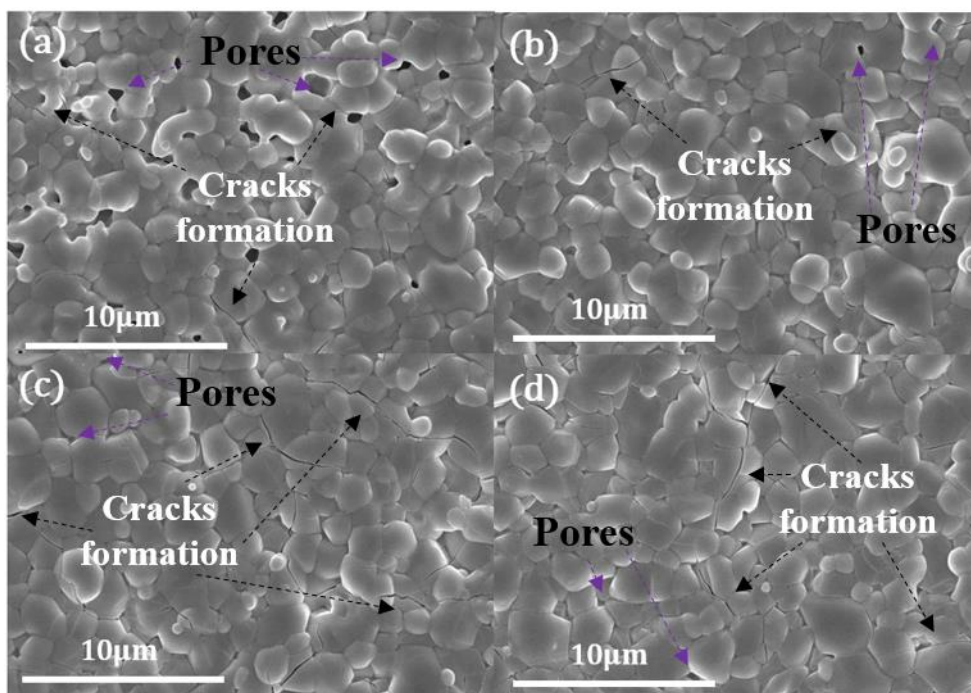


Figure.4. FE-SEM images of LiTaSiO₅ SEs sintered for (a) 6 h, (b) 12 h, (c) 18 h, and (d) 24 h.

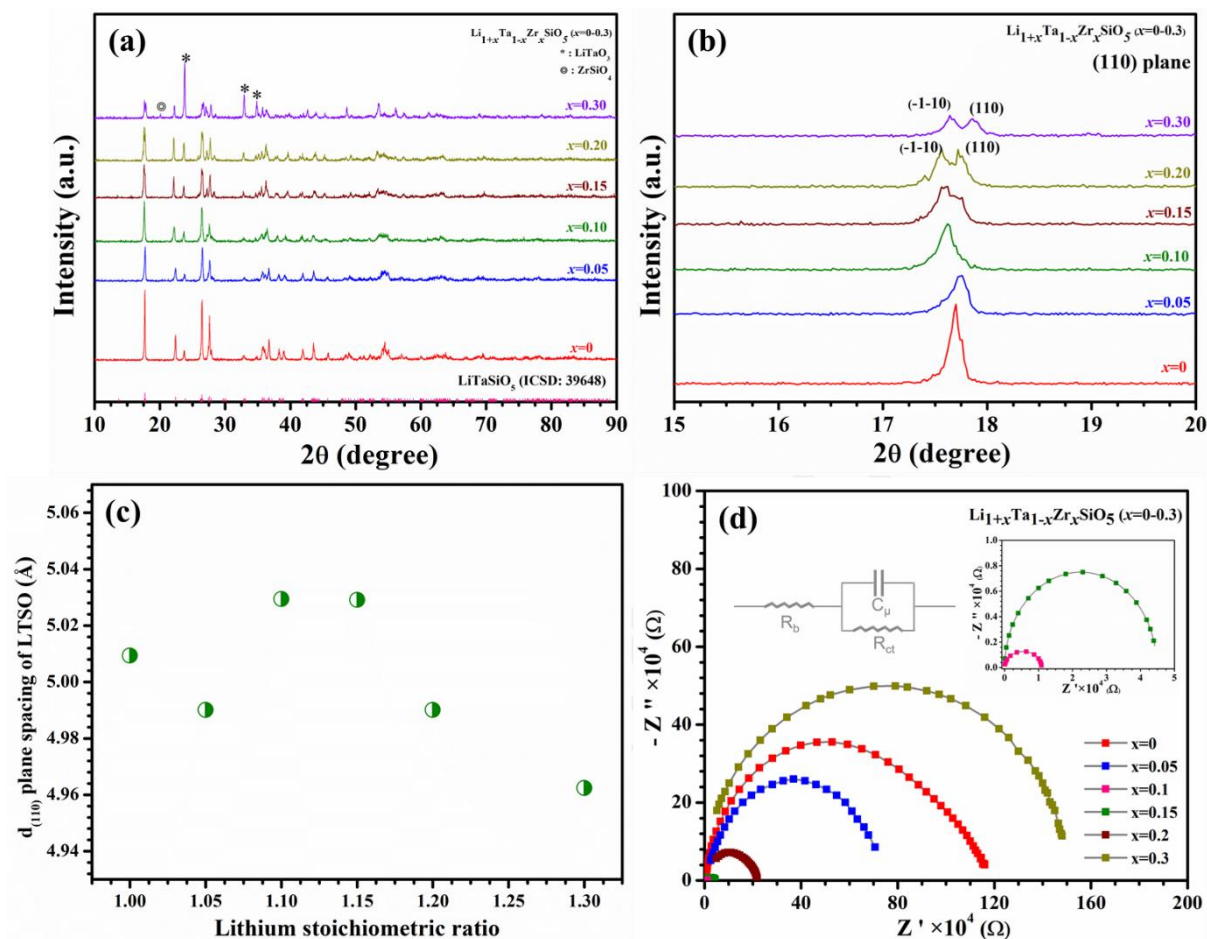


Figure.5. (a) XRD patterns of $\text{Li}_{1+x}\text{Ta}_{1-x}\text{Zr}_x\text{SiO}_5$ (x = 0-0.3) materials with different compositions, (b) graph of the (110) plane, (c) $d_{(110)}$ plane spacing of $\text{Li}_{1+x}\text{Ta}_{1-x}\text{Zr}_x\text{SiO}_5$ (x=0-0.3) SEs with different compositions, and (d) EIS curves of $\text{Li}_{1+x}\text{Ta}_{1-x}\text{Zr}_x\text{SiO}_5$ (x=0-0.3) SEs with different compositions.

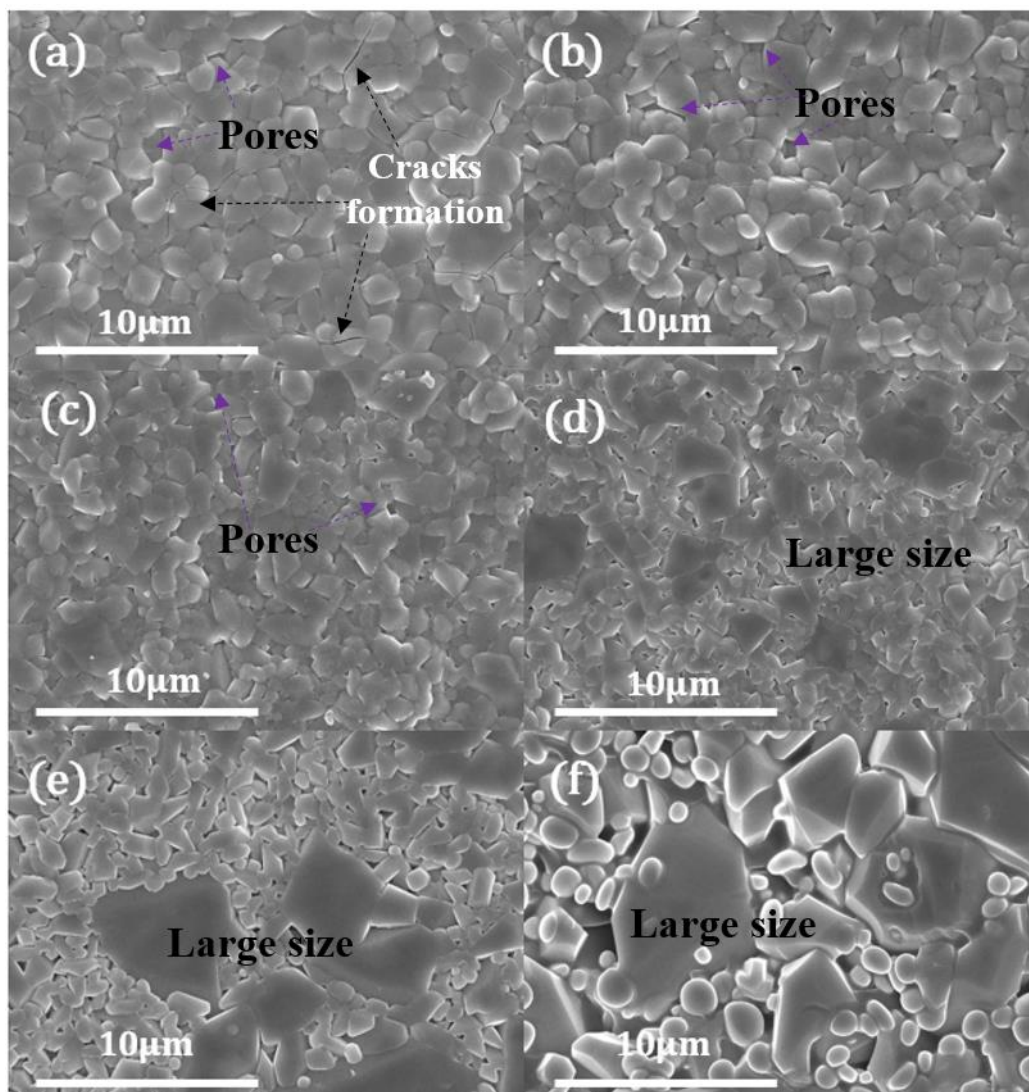


Figure.6. FE-SEM images of $\text{Li}_{1+x}\text{Ta}_{1-x}\text{Zr}_x\text{SiO}_5$ materials for (a) $x = 0$, (b) $x = 0.05$, (c) $x = 0.1$, (d) $x = 0.15$, (e) $x = 0.2$, and (f) $x = 0.3$.

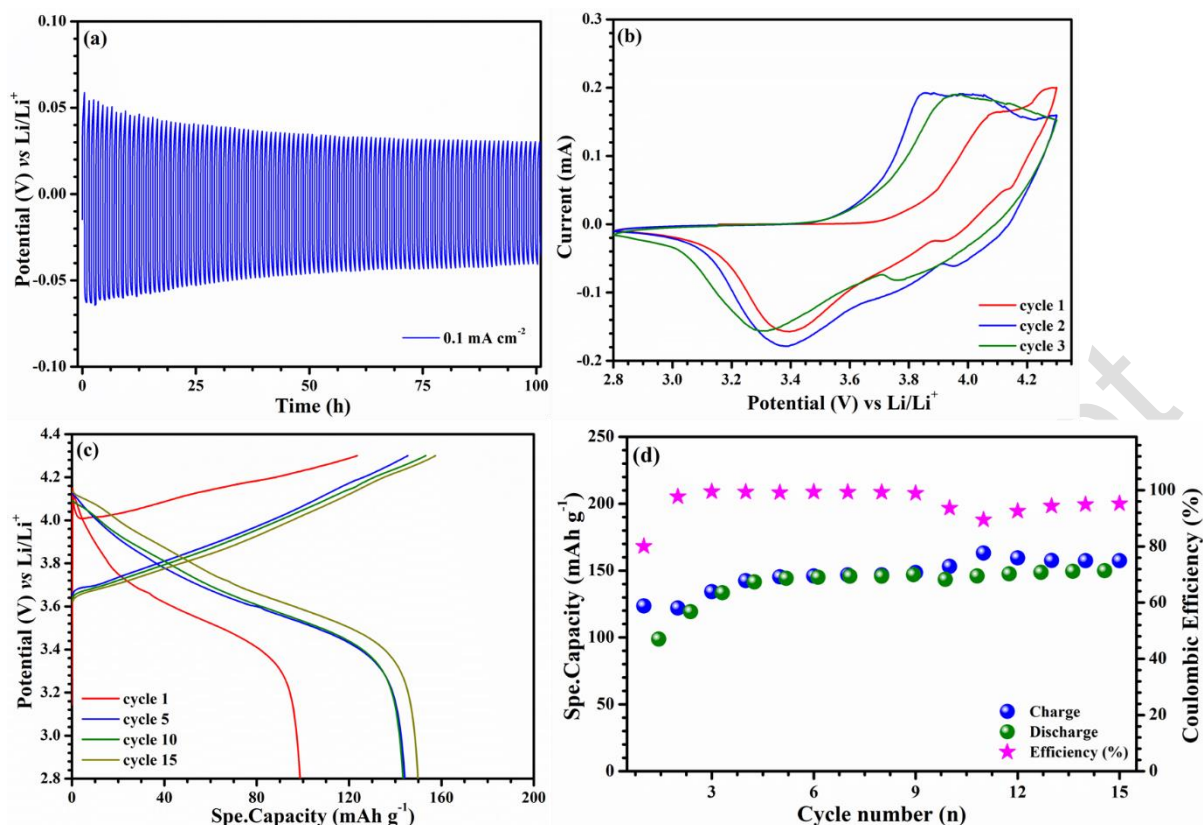


Figure 7. (a) Galvanostatic charge-discharge curve of the Li//LE-LTZSO-LE//Li symmetric cell with current density 0.1 mA cm⁻² (b) Cyclic voltammetry at 0.1 mV s⁻¹ scan rate, (c) Charge-Discharge curve of the cell for selected cycles and (d) Cycle life of the Li//LE-SE-LE//NCM811 cell at 0.2 C rate and all the electrochemical studies were done at 25 °C.

Table 1: Lattice parameters of LTSO SEs prepared at different sintering temperatures from the XRD data displayed in **Figure 1**

Temperature (°C)	a(Å)	b(Å)	c(Å)	V(Å ³)
ICSD: 39648	7.396	7.93	7.444	381.1857
1000	7.3892	7.9308	7.4238	379.8392
1050	7.396	7.9357	7.4344	380.9678
1100	7.3957	7.9319	7.4344	380.7699

Table 2: Lattice parameters of LTSO SEs sintered for different durations from the XRD data displayed in Figure 3.

Temperature (°C)	a (Å)	b (Å)	c (Å)	v (Å ³)
ICSD: 39648	7.396	7.93	7.444	381.1857
6 h	7.396	7.9357	7.4344	380.9678
12 h	7.3955	7.9314	7.4344	380.7356
18 h	7.3871	7.9228	7.4397	380.1616
24 h	7.4111	7.9457	7.4504	383.0492

Table 3: Lattice parameters of LTSO SEs sintered for different durations from the XRD data displayed in Figure 3

Temperature (°C)	Average grain size (nm)
6 h	42.37
12 h	46.32
18 h	44.73
24h	34.39

Table 4: Lattice parameters of LTSO SEs prepared with different compositions based on the XRD data presented in Figure 3.

$\text{Li}_{1+x}\text{Ta}_{1-x}\text{Zr}_x\text{SiO}_5$ ($x = 0-0.3$)	a (Å)	b (Å)	c (Å)	V (Å ³)
ICSD: 39648	7.396	7.93	7.444	381.1857
$x = 0$	7.3955	7.9314	7.4344	380.7356
$x = 0.05$	7.3871	7.9338	7.4504	381.2369
$x = 0.10$	7.4043	8.0082	7.4771	387.0913
$x = 0.15$	7.373	8.0283	7.4933	387.2605
$x = 0.20$	7.3646	8.0246	7.4291	383.3266
$x = 0.30$	7.3347	7.9915	7.4291	380.1955

Table. 5. ICP-OES analysis results of $\text{Li}_{1+x}\text{Ta}_{1-x}\text{Zr}_x\text{SiO}_5$ ($x = 0 - 0.3$) materials.

x	Li/O	Ta/O	Zr/O	Si/O	Formula
0	1.02	0.99	0	0.99	$\text{Li}_{1.02}\text{Ta}_{0.99}\text{SiO}_5$
0.05	1.06	0.95	0.04	0.98	$\text{Li}_{1.06}\text{Ta}_{0.95}\text{Zr}_{0.04}\text{Si}_{0.98}\text{O}_5$
0.1	1.11	0.90	0.09	0.95	$\text{Li}_{1.11}\text{Ta}_{0.9}\text{Zr}_{0.09}\text{Si}_{0.95}\text{O}_5$
0.15	1.16	0.86	0.13	0.98	$\text{Li}_{1.16}\text{Ta}_{0.86}\text{Zr}_{0.13}\text{Si}_{0.98}\text{O}_5$
0.2	1.21	0.80	0.19	0.96	$\text{Li}_{1.21}\text{Ta}_{0.80}\text{Zr}_{0.19}\text{Si}_{0.96}\text{O}_5$

Table. 6. Ionic conductivities and relative densities of $\text{Li}_{1+x}\text{Ta}_{1-x}\text{Zr}_x\text{SiO}_5$ ($x = 0\text{--}0.3$) SEs having different compositions.

Solid electrolyte	Ionic conductivity (S cm^{-1})	Relative density (%)
LiTaSiO_5	1.78×10^{-7}	79.5
$\text{Li}_{1.05}\text{Ta}_{0.95}\text{Zr}_{0.05}\text{SiO}_5$	2.97×10^{-7}	84.7
$\text{Li}_{1.1}\text{Ta}_{0.9}\text{Zr}_{0.1}\text{SiO}_5$	2.01×10^{-5}	90.7
$\text{Li}_{1.15}\text{Ta}_{0.85}\text{Zr}_{0.15}\text{SiO}_5$	5.14×10^{-6}	90.3
$\text{Li}_{1.2}\text{Ta}_{0.8}\text{Zr}_{0.2}\text{SiO}_5$	1.03×10^{-6}	89.3
$\text{Li}_{1.3}\text{Ta}_{0.7}\text{Zr}_{0.3}\text{SiO}_5$	1.55×10^{-7}	89.8

5. References

1. B. Ramkumar, S.Y. Kim, C.W. Nam, V. Aravindan and Y.S. Lee. *Electrochim Acta*. **2020**, 359, 136955.
2. B. Ramkumar, V. Aravindan, H. Ramasamy, K.V. Ajeya, J.G. Ryu, H.Y. Jung and Y.S. Lee. *Solid State Sci*. **2022**, 132, 106958.
3. B. Ramkumar, S. Yuvaraj, S. Surendran, K. Pandi, R. Harivignesh, Y.S. Lee and R.K. Selvan. *J Phys Chem Solids*. **2018**, 112, 270-279.
4. J.G. Ryu, R. Balasubramaniam, V. Aravindan, S. Park, S.J. Cho and Y.S. Lee. *ACS Appl Mater Interfaces*. **2024**, 16(1), 761-771.
5. H. Kim, D.I. Kim, W.S. Yoon. *J Electrochem Sci Technol*. **2022**, 13(1), 32-53.
6. S.J. Tan, X.X. Zeng, Q. Ma, X.W. Wu, Y.G. Guo. *Electrochem Energy Rev*. **2018**, 1(2), 113-138.
7. R. Balasubramaniam, C.W. Nam, V. Aravindan, D. Eum, K. Kang and Y.S. Lee. *ChemElectroChem*. **2021**, 8(3), 570-576.
8. R. Balasubramaniam, C.W. Nam, V. Aravindan, J.C. Seol, K.V. Ajeya, H.Y. Jung and Y.S. Lee. *ChemElectroChem*. **2022**, 9(14), e202200317.
9. J.C. Seol, R. Balasubramaniam, V. Aravindan, R. Thangavel and Y.S. Lee. *J Alloys Compd*. **2022**, 927, 167077.
10. S.B. Lee and R. Balasubramaniam. *J Ind Eng Chem*. **2022**, 110, 262-273.
11. T.M. Nguyen, J. Suk and Y. Kang. *J Electrochem Sci Technol*. **2019**, 10(2), 250-255.
12. J. Lee, D.C. Shin, Y.W. Song, D. Hwang, M.Y. Kim, H. Jeong, D.C. Shin and J. Lim. *J Electrochem Sci Technol*. **2022**, 13(2), 199-207.
13. L. Ni, Z. Wu and C. Zhang. *Materials (Basel)*. **2021**, 14(7), 1671.
14. C. B. Lim and Y.J. Park. *J Electrochem Sci Technol*. **2020**, 11(4), 411-420.
15. J. Y. Lee, Y.J. Park. *J Electrochem Sci Technol*. **2022**, 13(3), 407-415.
16. R. Murugan, V. Thangadurai and W. Weppner. *Angew Chemie - Int Ed*. **2007**, 46(41), 7778-7781.

17. H. Aono, E. Sugimoto, Y. Sadaoka, N. Imanaka and G.Y. Adachi. *Solid State Ionics*. **1990**,40-41(1),38-42.
18. Y. Inaguma, L. Chen, M. Itoh, T. Nakamura. *Solid State Commun*. **1993**,86(10), 689-693.
19. N. Kamaya, K. Homma, Y. Yamakawa, M. Hirayama, R. Kanno, M. Yonemura, T. Kamiyama, Y. Kato, S. Hama, K. Kawamoto and A. Mitsui. *Nat Mater*. **2011**,10(9), 682-686.
20. R. Rajagopal, K.S. Ryu. *Chem Eng J*. **2020**, 402, 126179.
21. K. Heo, J. Im, J.S. Lee, J. Jo, S. Kim, J. Kim and J. Lim. *J Electrochem Sci Technol*. **2020**, 11(3), 282-290.
22. F. Chen, G. Zhang, Y. Zhang, S. Cao and J. Li. *J Electrochem Sci Technol*. **2022**, 13(3), 362-368.
23. H.M. Choi, S.J. Jun, J. Lee, M.H. Ryu, H. Shin and K.N. Jung. *J Electrochem Sci Technol*. **2023**, 14(1), 85-95.
24. S. Xiong, X. He, A. Han, Z. Liu, Z. Ren, B. McElhenny, A.M. Nolan, S. Chen, Y. Mo and H. Chen. *Adv Energy Mater*. **2019**, 9, 1803821.
25. Y. Wang, W.D. Richards, S.P. Ong, L.J. Miara, J.C. Kim, Y. Mo and G. Ceder. *Nat Mater*. **2015**,14,1026-1031.
26. X. He, Y. Zhu and Y. Mo. *Nat Commun*. **2017**,8, 15893.
27. X. He, Q. Bai, Y. Liu, A.M. Nolan, C. Ling and Y. Mo. *Adv Energy Mater*. **2019**, 9(43), 1902078.
28. Q. Wang, J.F. Wu, Z. Lu, F. Ciucci, W.K. Pang and X. Guo. *Adv Funct Mater*. **2019**, 29(37), 1904232.
29. E.A. Genkina and B.V. Mill, *Kristallografiya*, **1992**, 37(6), 1424-1428
30. J. Choi, S.Y. Lee, S. Yoon, K.H. Kim, M. Kim and S.H. Hong. *ChemSusChem*. **2019**, 12(11), 2439-2446.
31. R. Jenkins, R.L. Snyder. *Introduction to X-ray Powder Diffractometry*. *Introduction to X-ray Powder Diffractometry*; Wiley, 1996.

32. S.J.L. Kang, Sintering Densification, Grain growth, and Microstructure, **2005**.
33. K. Waetzig, C. Heubner and M. Kusnezoff. *Crystals*. **2020**, 10, 408.
34. R.L. Coble. *J Appl Phys*. **1963**, 34(6), 1679-1682.
35. M.P. Groover. Fundamentals of Modern Manufacturing Materials, Processes, and Systems, 4th Edition, Wiley, John Wiley & Sons, INC. **2010**.
36. C.A. Alima, V.B. Luciano, L.B.M. Jorge and D.S. José. *Int J Eng Res*. **2016**, 5(12), 290-295.
37. Q. Cheng, Y. Wang, J. Zhang, A.N. Conejo and Z. Liu. *Chem Eng Sci*. **2022**, 262, 118038.
38. X. Li and K. Lu. *Acc. Mater. Res*. **2021**, 2(2), 108-113.
39. J. Choi, S.Y. Lee, S. Yoon, K.H. Kim, M. Kim and S.H. Hong. *ChemSusChem*. **2019**, 12(11), 2439-2446.
40. F.K. *Zeitschrift, Kristallgeometrie, kristallphysik, Kristallchemie*, **1926**, 63, 247-254.
41. M.J. Akhtar and S. Waseem, Solid state sciences, **2003**, 5, 541-548.
42. M. Rahimian, N. Ehsani, N. Parvin and H.R. Baharvandi. *J Mater Process Technol*. **2009**, 209(14), 5387-5393.
43. R.M. German. Sintering Theory and Practice. **1996**, Wiley
44. R.M. German, Powder metallurgy of iron and steel. **1998**, John Wiley & Sons